Single-point structure tensors in turbulent channel flows with smooth and wavy walls

Junlin Yuan,[1, a)] Aashwin Ananda Mishra,[2] Giles Brereton,[1] Gianluca Iaccarino,[2] and Magnus Vartdal[3]

[1)]*Department of Mechanical Engineering, Michigan State University, East Lansing, MI 48824, USA*

[2)]*Center for Turbulence Research, Stanford University, Stanford, CA 94305, USA*

[3)]*Norwegian Defence Research Establishment (FFI), Kjeller NO-2027, Norway*

(Dated: 27 December 2021)

A long-standing problem in turbulence modeling is that the Reynolds stress tensor alone is not necessarily sufficient to characterize the transient and non-equilibrium behaviors of turbulence under arbitrary mean deformation or frame rotation. A more complete single-point characterization of the flow can be obtained using the structure Dimensionality, Circulicity, and Inhomogeneity tensors. These tensors are one-point correlations of local stream vector gradients and carry non-local information regarding the structure of the flow field. We explore the potential of these tensors to improve understanding of complex turbulent flows using direct numerical simulation of flows in channels with a smooth wall and a two-dimensional sinusoidal wavy wall. To enforce no-slip and no-penetration conditions at wavy-wall boundaries, an immersed boundary method for the stream vector Poisson equation was adopted within the framework of F. S. Stylianou, R. Pecnik, and S. C. Kassinos, *Comput. Fluids*, 106, 54–66 (2015). Results show that the effects of wall waviness on the inclination and aspect ratio of the two-point velocity correlation near the wall are reproduced qualitatively by their corresponding single-point tensor representations. In the outer layer, good quantitative agreement is achieved for both parameters. Additional observations on the structural changes of turbulence due to wall waviness and their relevance to turbulence modeling with surface roughness are discussed. The findings of this investigation suggest that single-point structure tensors can be appended to the modeling basis for inhomogeneous flows with geometrically complex boundaries, such as rough-wall flows, to develop improved turbulence models.

[a)]Electronic mail: junlin@egr.msu.edu

I. INTRODUCTION

Many turbulent flows in engineering and environmental applications are both at high Reynolds numbers and over rough surfaces. For example, in turbomachines the blade surfaces undergo wear due to pitting, erosion, deposition, etc., which changes their surface roughness. Assessing the ensuing degradation in performance requires accounting explicitly for this wear in simulations. Similarly, accounting for the effects of ice accretion on the leading edges of airfoils is essential to accurate prediction of airfoil performance. The use of ablative materials on re-entry-vehicle nose cones can also result in significant changes to their surface roughness. Computational Fluid Dynamics (CFD) simulations must therefore account for effects of roughness to estimate accurately design parameters such as heat transfer coefficients. In wall bounded flows, surface roughness can lead to a substantial increase in form drag, associated with a greater intensity of pressure and velocity fluctuations. In each of the preceding examples, the dynamics of the flow is complicated further by additional factors such as pressure gradients, unsteadiness, surface curvature, and complex geometries. In spite of rapid increases in computational resources, direct numerical simulations (DNS) of such complex engineering flows remain impractical. At present and for the foreseeable future, the only pragmatic computational approach to simulating such non-equilibrium turbulent boundary layers is to use single-point closures in the vicinity of the wall or throughout the boundary layer.

The ability of most single-point closures to model different features of turbulent flows is limited by the fact that the state of the turbulent flow field is expressed only in terms of the Reynolds stresses, as in the case of a second-moment closure approach. This corresponds to a coarse-grained[1] description of the turbulent flow field and limits the features of turbulence that such models can potentially replicate. For instance, Sagaut and Cambon[2] have shown that in the presence of background rotation, Reynolds stress anisotropy should be decomposed into directional and polarization anisotropies, each of which is affected very differently by the pressure-velocity correlations through the action of the Coriolis force. Additionally, this coarse-grained description introduces uncertainty into the modeling problem[3,4] as all turbulent flows with the same Reynolds stress need not evolve identically under the same strain-rate histories. Kassinos and Reynolds[5] have shown that using just the Reynolds stresses to characterize the turbulent flow field limits models by eschewing information regarding dynamically important physics. The Reynolds stresses carry only information on the componentality of turbulence—the relative strengths of different velocity com-

ponents. Kassinos, Reynolds, and Rogers[6] introduced additional tensors to the modeling basis that add important information to improve turbulence model predictions in homogeneous turbulent flows. These tensors include the Structure Dimensionality tensor, which characterizes the relative uniformity of the turbulence structure in different directions, and the Circulicity tensor, which characterizes the large-scale circulation around a particular axis. These tensors are used to describe the structure of the turbulent flow field and their definitions are given in Section II C.

While seminally important in homogeneous flows, the aforementioned effects of coarse-graining are further exacerbated when turbulent flows are inhomogeneous, in regions such as the vicinity of a smooth wall. To explore the ability of these structure tensors to model inhomogeneous flows, it is important to clarify to what extent these tensors represent the same information in homogeneous and inhomogeneous flows. For example, it can be shown[7] that the Dimensionality tensor represents exactly the characteristics of the two-point velocity correlation in homogeneous turbulence. Specifically, the tensor eigenvalue ratio represents the aspect ratio of the two-point velocity-correlation contour, and the tensor principal-axes inclination represents the contour rotation. This is true under the assumptions of homogeneous turbulence for the scales in the inertial subrange. It is not clear whether such representations still apply near a wall, where turbulence is inhomogeneous and the local Reynolds number is often low.

In this study, we analyze the structure-tensor representation of turbulence above smooth and wavy walls using half-channel DNS simulations. The structural characteristics are compared with the corresponding information represented by the same tensors in the case of homogeneous turbulence. We also analyze whether these tensors capture near-surface changes in the structure of turbulence caused by wall waviness—a simple, two-dimensional surface roughness[8,9]. Section II summarizes the simulation parameters and provides calculation details of the stream vector and the single-point tensors, which are validated in Section III. In Section IV, we compare characteristics of the actual coherent motions with the tensors and reduce the tensors to principal information that can be used for modeling purposes. An overarching objective of many turbulence modeling efforts is to improve the fidelity of closures by integrating a higher degree of underlying physics within the closure model. To this end, a promising approach is to append to the modeling basis tensors that carry information on features of turbulence physics that are difficult to represent in existing models. In this context, single-point structure tensors appear to be very promising as they are effective measures of non-local characteristics of homogeneous turbulence[5]. In this paper, we show that for complex inhomogeneous turbulence, these tensors contain qualitative information

on the structure of the turbulent flow field and we quantify their behavior in the vicinity of a wavy wall.

II. PROBLEM FORMULATION AND METHODOLOGIES

A. Modeling background

Turbulence theory and the modeling of flows at high Reynolds numbers with complex inhomogeneity are of considerable importance. The atmospheric boundary layer[10] and flows over urban and natural canopies[11] are ubiquitous examples of turbulent flows over rough surfaces. Virtually all surfaces of engineering and scientific interest have some roughness and flows over them can be fundamentally different from their smooth-wall counterparts, in terms of their underlying physics and their engineering ramifications. With respect to the former, the innate physics of turbulence close to the wall is affected strongly by roughness. For instance, depending on the roughness height, the surface roughness can either interfere with the dynamics of the buffer-layer viscous production mechanism or interrupt it completely. In terms of flow variables, roughness leads to changes in the mean velocity profiles near the wall, in length scales and in turbulent kinetic energy distributions[12]. With respect to the latter, transition to turbulence can be promoted by surface roughness[13]. Surface roughness can lead to changes in both the flow's coherent structures and its behavior far from the wall[14]. It can also substantially enhance the Nusselt number in devices such as heat exchangers[15]. Moreover, the physics underlying these phenomena can be complicated. For example, the augmentation of heat transfer by roughness is a consequence of an increase in surface area due to roughness, together with increased heat diffusion through roughness-enhanced turbulent motion. Consequently, complex inhomogeneity leads to significant changes in the physics of turbulent flows that may be difficult to describe with existing turbulence models.

Established turbulence models like Reynolds stress closures are typically formulated for homogeneous turbulence, while eddy viscosity models are usually developed and calibrated for smooth walled flows. The application of such turbulence closures to rough surface flows typically requires the use of ad hoc techniques. For instance, the equivalent sand grain approach introduces the sand-grain roughness height as a new parameter for the turbulence model, which enables the enhancement of turbulence in the near-wall region, to increase the momentum transport toward the wall and to reproduce the drag increase. However, there is a schism between the physics under-

lying these phenomena and the manner in which such approaches reproduce them. For example, equivalent sand-grain roughness models increase the frictional drag even though it arises predominantly through pressure forces on roughness elements. Alternatively, various correction terms have been appended to established turbulence models to account for roughness[16–18]. In addition to being largely empirical, such corrections suffer from a lack of robustness and universality. For instance, the correction by Wilcox [19] profoundly affects the flow over smooth surfaces and causes unrealistically low eddy-viscosity values over regions of high roughness. In the same vein, different correction terms have to be formulated to account for the drag increase at the wall due to roughness and the heat transfer augmentation by roughness, with complementary wall functions for each correction etc., resulting in a cumbersome framework that may lack robustness and does not offer consistent fidelity across different flows, or even across all regions of a single turbulent flow. In this light, accounting for the effects of surface roughness in Reynolds-Averaged Navier-Stokes (RANS) simulations has been described as the "Achilles heel of CFD"[20].

In contrast to conventional closure formulations, elliptic relaxation models have shown some success in predicting turbulence over rough walls[21–23]. The $v^2 - f$ closure in these studies includes terms that combine the effects of the near-wall velocity-pressure gradient correlation and the anisotropic dissipation rate and, by extension, the near-wall stress anisotropy and the non-local pressure-strain effects. The need for any near wall damping functions is obviated by incorporating near-wall turbulence anisotropy and non-local pressure-strain effects via an elliptic relaxation equation that captures the non-local, wall-blocking effects. This facet is critical in the computation of strongly heterogeneous turbulent flows such as rough wall flows, enabling more accurate prediction of heat transfer, skin friction, and turbulent boundary layer separation. Consequently, the addition of information regarding the turbulence structure may potentially enable better modeling of turbulence over complex inhomogeneity. In an analogous scenario, appending turbulence structure tensors to the modeling basis should improve the modeling of non-local physics in second moment closures. In this investigation, we analyze whether such structure tensors may aid turbulence modeling over complex inhomogeneities. We focus on the nature of information provided by such tensors about turbulence in the vicinity of rough or wavy surfaces, the extent of this information and its distribution over individual tensors.

Wall	Re_τ	k_s^+	k_c/δ	$(L_x, L_z)/\delta$	(n_i, n_j, n_k)	$(\Delta x^+, \Delta z^+)$	$(\Delta y^+_{\text{min}}, \Delta y^+_{\text{max}})$	Tu_τ/δ	Δt^+
Smooth	1000	0	0	(6,3)	(512,256,512)	(11.7,5.8)	(0.3, 9.9)	85	0.03
Wavy	1000	75	0.05	(6,3)	(1024,226,512)	(6.0,6.0)	(0.9, 10.6)	86	0.04

TABLE I. Half-channel DNS simulation summary. Superscript + indicates normalization using friction velocity u_τ and viscous length scale δ_ν. L_x and L_z are domain sizes, δ is the channel half height, k_c is the roughness crest height, T is the total simulation time and Δt is the time step size. $Re_\tau = u_b\delta/\nu$, where u_b is bulk velocity. k_s is the equivalent sand-grain height, which relates the drag of a roughness to that of the sand-grain roughness studied by Nikuradse[24].

B. Simulation data

The DNS simulations of this investigation were performed using a well-validated code that solved the governing equations on a staggered grid using second-order, central differences for all terms, second-order accurate Adams-Bashforth semi-implicit time advancement, and Message Passing Interface parallelization. For the wavy-wall case, an immersed boundary method (IBM) based on the volume-of-fluid approach is used to impose no-slip boundary conditions at the surface. The Neumann boundary condition of pressure at the solid-fluid interface is not explicitly imposed. Detailed implementation and validation are provided by Yuan and Piomelli[25,26].

The parameters of the DNS simulations are summarized in Table I. Here, x_1, x_2, and x_3 (or x, y, and z) are, respectively, the streamwise, wall-normal, and spanwise directions, and u_j (or u, v, and w) are the velocity components in those directions. For both cases, a half channel is simulated to limit computational cost. Such approximation of a full channel as a half channel is widely used in the literature when the focus of the study is not near the channel center line (for example, see Scotti[27]). No-slip and symmetric boundary conditions ($\partial u/\partial y = 0$, $\partial w/\partial y = 0$, $v = 0$) are applied to the bottom and top boundaries of the simulation domain respectively, and periodic conditions are used in x and z. Following previous publications on rough-walled channel flows using this code[26,28,29], a constant pressure gradient is applied to drive the flow. The constant pressure gradient is imposed inside both fluid and solid; in solid, it is balanced by the IBM forcing. Note also that the imposed pressure gradient is the gradient of the space- and time-averaged pressure. The pressure that is solved is the sum of the form-induced pressure (see Eq. 1) and the turbulent fluctuating pressure.

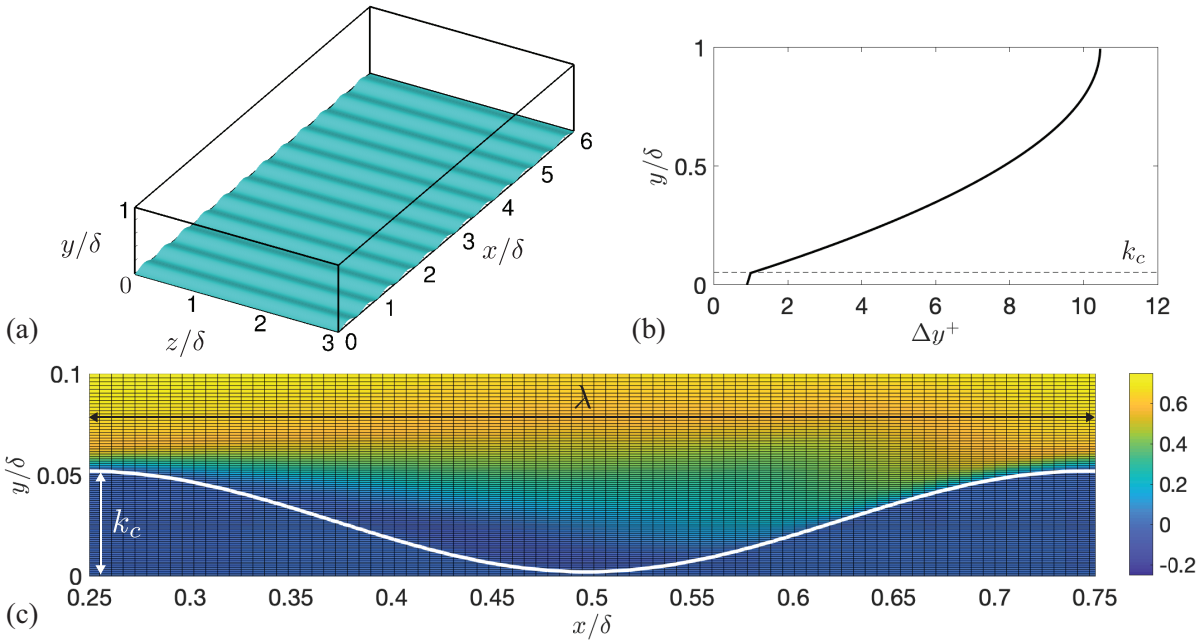

FIG. 1. (a) Simulation domain and the wall geometry of the wavy-wall case. (b) Wall-normal grid sizes in wall units. (c) Contour of time-averaged streamwise velocity overlaid with the mesh to show resolution of local shear layers. λ is the wavelength of the wavy wall.

Channel flows with two-dimensional sinusoidal wavy walls have been studied extensively. Experimental and numerical studies showed that, if the wave height ($2a$, equivalent to k_c herein) to length (λ) ratio (also called wave slope) is large ($2a/\lambda \geq 0.10$), the flow exhibits a large, unsteady, recirculation zone downstream of the wave crest[8,30–32]. This flow can be separated into two zones: an outer layer, for which the wavy wall is considered as an equivalent roughness, and an inner region. The latter is characterized by the presence of a region of reverse flow developing downstream of the wave crest, forming an intense shear layer above the recirculation region, and a very thin boundary layer that develops beyond the reattachment point. Away from the wall region, the logarithmic mean velocity profile, the Reynolds stresses and the two-point velocity correlations appear not to be affected by the wavy wall[9,33]. Therefore, such a wall geometry is equivalent to large-scale two-dimensional roughness. For the waviness simulated here, $2a/\lambda$ is set to 0.10 to generate significant separation regions near the wall and the peak-to-trough height k_c is 0.05δ (or $k_c^+ = 50$) to yield a flow at the lower limit of the fully rough regime for this surface (the full rough regime is reached at $k_c^+ = 60$ for $2a/\lambda = 0.10$[9]), while maintaining a clear scale separation between the roughness height and the channel height. The roughness wavelength λ is 0.5δ. Here

$y = 0$ is defined as the lowest elevation of the rough surface and the zero-plane location d is defined as the centroid of the rough-wall drag distribution[34] which was at 0.031δ in these simulations.

For the wavy-wall case, the simulation domain, wall geometry, grid sizes in y and the spatial resolution of the local shear layers are shown in Fig. 1. The grid sizes in wall units are smaller than the DNS study of Maas and Schumann[35], who used $\Delta x^+ = \Delta z^+ \approx 10$ and $\Delta y^+_{\text{min}} = 1.6$ and obtained results that compared well with the experimental measurements of Hudson[36]. A domain with $L_x \geq 2\lambda$ and $L_z \geq \lambda$ has been shown sufficient for an accurate evaluation of the inner-layer statistics[37]. Keylock et al.[38] commented that L_x of more than 3λ is required to ensure that the x periodic boundary condition does not impact on the inferred dynamics of large-scale vortical structure. The present L_x value of 12λ is thus considered sufficient. For both simulations, the maximum Δy^+ and the total simulation time are comparable to DNS of channel flows in the literature (see, for example, Sillero et al.[39]).

Near the wall, roughness leads to spatial heterogeneity in the flow. Time-averaged perturbations in space are separated from turbulent fluctuations using the double-averaging decomposition introduced by Raupach and Shaw[40],

$$\theta(x_i,t) = \langle\overline{\theta}\rangle(y) + \widetilde{\theta}(x_i) + \theta'(x_i,t), \tag{1}$$

where θ is an instantaneous flow variable, $\langle\theta\rangle$ is the intrinsic spatial average in the (x,z) plane, $\langle\theta\rangle = 1/A_f \int_{A_f} \theta\, dA$ (where A_f is the area occupied by fluid at the corresponding y), $\overline{\theta}$ is the average in both time and z, $\theta' = \theta - \overline{\theta}$ is the instantaneous turbulent fluctuation, and $\widetilde{\theta} = \overline{\theta} - \langle\overline{\theta}\rangle$ is the form-induced fluctuation. The double-averaging technique has been used in the rough-wall turbulence literature to distinguish between turbulent and form-induced fluctuations by, for example, Coceal, Thomas, and Belcher[41], Pokrajac, McEwan, and Nikora[42] and Mignot, Bartheleemy, and Hurther[43]. This decomposition is applied to flow data for both smooth and wavy wall simulations.

C. Structure-tensor calculation

1. Smooth-wall channel

The structure tensors are second-order moments of the three-dimensional instantaneous stream vector ψ_i which is determined from the Poisson equation

$$-\frac{\partial^2 \psi_i}{\partial x_j \partial x_j} = \omega_i, \tag{2}$$

where ω_i is the vorticity vector and ψ_i is related to u_i as $u_i = \varepsilon_{ijk}\psi_{k,j}$, where ε_{ijk} is the Levi-Civita symbol.

Periodic boundary conditions are applied to ψ_i in x and z. Following Stylianou, Pecnik, and Kassinos[44], the y boundary conditions of Eq. (2) are imposed as (no summation among Greek letters)

$$n_\alpha \psi_\alpha + n_\beta \psi_\beta + n_\gamma \psi_\gamma = 0, \tag{3}$$

$$-n_\alpha \frac{\partial \psi_\beta}{\partial x_\alpha} - n_\gamma \frac{\partial \psi_\beta}{\partial x_\gamma} = -n_\alpha \frac{\partial \psi_\alpha}{\partial x_\beta} - n_\gamma \frac{\partial \psi_\gamma}{\partial x_\beta} + \varepsilon_{\beta jk} n_j u_k, \tag{4}$$

and

$$-n_\alpha \frac{\partial \psi_\gamma}{\partial x_\alpha} - n_\beta \frac{\partial \psi_\gamma}{\partial x_\beta} = -n_\alpha \frac{\partial \psi_\alpha}{\partial x_\gamma} - n_\beta \frac{\partial \psi_\beta}{\partial x_\gamma} + \varepsilon_{\gamma jk} n_j u_k, \tag{5}$$

where n_α, n_β and n_γ are the components of the unit normal vector of the surface pointing out of the fluid domain. Index α corresponds to the maximum absolute component among the three (i.e. $|n_\alpha| > |n_\beta|$, $|n_\gamma|$), while the remaining indices, β and γ, are such that a right handed coordinate system is formed. Each component of ψ_i and ω_i is defined at the cell center. Equation (2) is recast as a system of linear equations using second-order central differencing (first-order one-sided differencing at the domain boundaries) and is solved using a successive over-relaxation (SOR) scheme.

The single-point structure tensors include the Reynolds stress (R_{ij}), Dimensionality (D_{ij}), Circulicity (F_{ij}), and Inhomogeneity (C_{ij}) tensors. They are defined by Kassinos, Reynolds, and Rogers[6] as

$$R_{ij} = \varepsilon_{ipq}\varepsilon_{jrs}\langle\overline{\psi'_{q,p}\psi'_{s,r}}\rangle,\ D_{ij} = \langle\overline{\psi'_{k,i}\psi'_{k,j}}\rangle,\ F_{ij} = \langle\overline{\psi'_{i,k}\psi'_{j,k}}\rangle,\ C_{ij} = \langle\overline{\psi'_{i,k}\psi'_{k,j}}\rangle \tag{6}$$

and so both temporal and spatial averaging of data is carried out to determine these tensor components. In this article, we follow the precedent of Kassinos, Reynolds, and Rogers[6] and classify these as single-point tensors.

Each tensor has a distinct physical meaning. C_{ij} represents the degree of spatial variation of statistical quantities, as $C_{ij} = \langle\overline{(\psi'_i\psi'_{k,j})_{,k}}\rangle$, which is zero for the case of homogeneous turbulence. As such, this tensor characterizes the degree of inhomogeneity of the turbulent flow field. The Structure Dimensionality tensor D_{ij} represents the relative uniformity of the structure of the turbulent flow field along different coordinate directions. Equivalently, this can be viewed as the distribution of turbulent kinetic energy along different directions in wavenumber space in a homogeneous flow. In contrast to the Dimensionality tensor, the Structure Componentality tensor

R_{ij} represents the relative strength of fluctuating velocity components along different coordinate directions. Lastly, $F_{\alpha\alpha}$ represents large-scale circulation around x_α, which can be shown by the fact that $\psi'_{\alpha,kk} = -\omega'_\alpha$ and that, if the flow is irrotational around x_α (i.e. $\omega'_\alpha = 0$ everywhere), $\psi'_\alpha =$ constant and consequently $\psi'_{\alpha,k} = 0$, in which case $F_{\alpha\alpha} = 0$. The connection between F_{ij} and the vorticity tensor $\langle\overline{\omega'_i\omega'_j}\rangle$ has been pointed out by Stylianou, Pecnik, and Kassinos[45] near the wall in a turbulent pipe flow.

Instead of using the classical definitions outlined in Eq. (6), we calculate R_{ij}, D_{ij}, and F_{ij} using an alternative approach given by Stylianou, Pecnik, and Kassinos[45], as

$$R_{ij} = \varepsilon_{imp}Q_{mjp},\ D_{ij} = \varepsilon_{imp}Q_{pmj} + C_{ij},\ F_{ij} = \varepsilon_{imp}Q_{jpm} + C_{ji}, \tag{7}$$

where $Q_{ijk} = -\langle\overline{u'_j\psi'_{i,k}}\rangle$ and C_{ij} is calculated according to its definition in Eq. (6). When calculating these tensors, the use of Eq. (7) results in less numerical error associated with the discretization of $\psi_{i,j}$[45]. The normalized forms of R_{ij}, D_{ij}, and F_{ij} are obtained by rescaling with their respective traces, as

$$r_{ij} = R_{ij}/R_{kk},\ d_{ij} = D_{ij}/D_{kk},\ f_{ij} = F_{ij}/F_{kk}. \tag{8}$$

In contrast, C_{ij} is normalized as

$$c_{ij} = C_{ij}/D_{kk}, \tag{9}$$

and is not rescaled by C_{kk} because C_{ij} is not positive semi-definite.

2. Immersed boundaries and the stream vector solver

For the wavy-wall case, the Poisson equation (2) for ψ_i is solved over the entire domain, including both the fluid and the solid. Two types of ψ_i boundary conditions are imposed: (1) domain boundary conditions that are the same as in smooth-wall channel flow; and (2) immersed boundaries on roughness. For the interface grid cells (the uppermost layer of grid cells of the immersed wall, either partially or fully solid), the wall boundary conditions (Eqs. (3)–(5)) are imposed with $\alpha = 2$, $\beta = 3$, and $\gamma = 1$, as the surface normal is predominantly in the y direction.

Currently, no local ψ_i reconstruction (similar to, for example, ghost-cell IBM[46]) is performed to ensure that the fluid-solid interface is sharp, as might be required for a higher numerical accuracy. The local normal vector of the immersed boundary $\vec{n}$ is obtained from the function $f(x,y,z) = 0$ that describes the plane locally tangent to the solid-fluid interface,

$$\vec{n} = \vec{\nabla}f/|\vec{\nabla}f|. \tag{10}$$

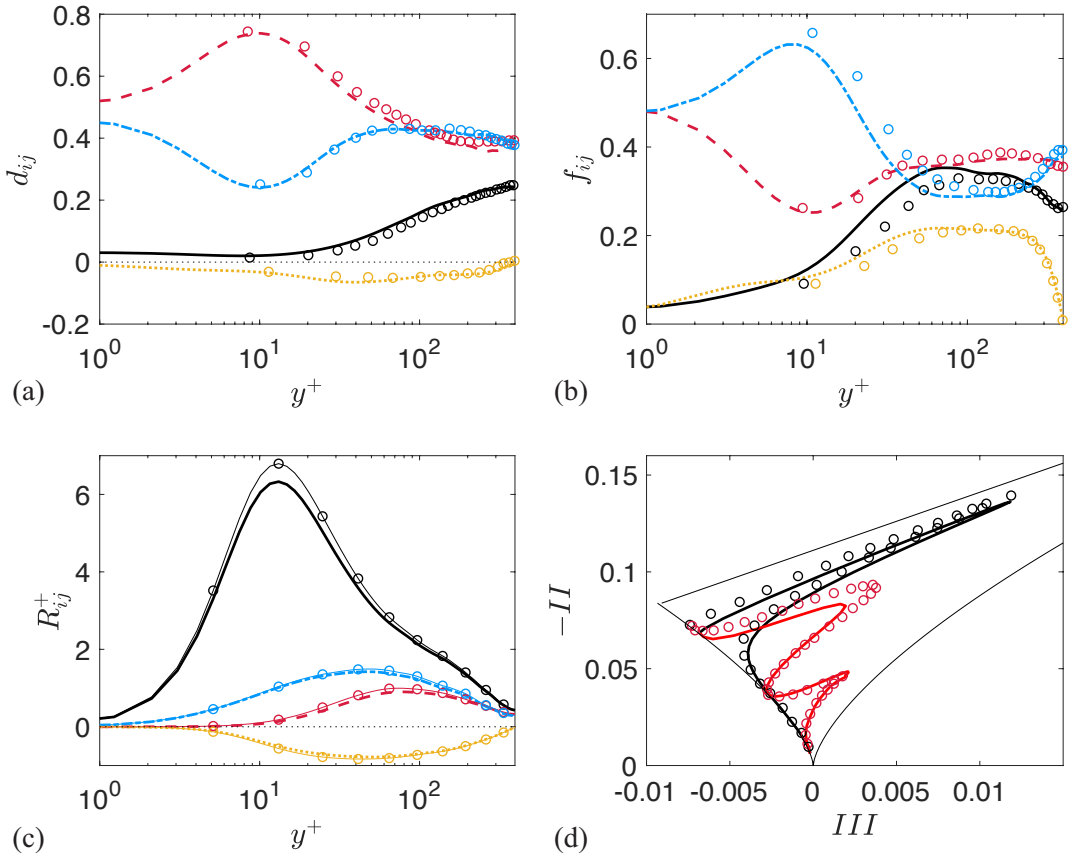

FIG. 2. (a-b) Self-normalized structure tensors obtained from smooth-wall channel flow LES with $Re_\tau = 395$. (c) R^+_{ij} from Eq. (7) (lines) versus error-free calculation (lines with symbols). Components: 11 (——), 22 (- - -), 33 (-- --), 12 (···). (d) Lumley triangle showing anisotropies of d_{ij} (——) and f_{ij} (——). Symbols in (a), (b), (d) are data from Vartdal[47].

Second-order central differencing is used to discretize Eqs. (10) to obtain $\vec{n}(\vec{x})$. It is then used in Eqs. (3)–(5) on the immersed boundary to enforce these boundary conditions, which are applied to interface grid cells explicitly at the end of each SOR iteration.

III. CODE VALIDATION

To validate the stream vector solver without immersed boundaries, ψ_i is calculated from large-eddy simulation (LES) data of a smooth-wall channel flow with $Re_\tau = 395$. The self-normalized tensors are compared with results obtained from a similar LES channel-flow simulation by Vart-

dal[47] in Fig. 2(a,b). The two LES simulations share the same domain size of $(2\pi \times 1 \times \pi)\delta$ and similar grid sizes, $(\Delta x, \Delta y_{\min}, \Delta z)^+ \approx (25, 0.6, 9)$. Good agreement is obtained for all components, the slight differences attributed to numerical error as Vartdal[47] calculated structural tensors through their definitions in Eq. (6) rather than Eq. (7). In Fig. 2(c), the Reynolds stress tensor obtained from Eq. (7) is compared with that obtained from the calculation of $R_{ij} = \langle \overline{u_i' u_j'} \rangle$ which is free of error from the ψ_i solver. The discrepancy quantifies the numerical error of the tensor calculation as up to 3% of the local R_{kk} value. A similar error range of $3-4\%$ of R_{kk} was also estimated by Stylianou, Pecnik, and Kassinos[45] from a pipe flow DNS with $Re_\tau = 180$. For the present DNS cases with $Re_\tau = 1000$, this error is estimated to be of up to 6% of R_{kk}. The anisotropy invariants of d_{ij} and f_{ij} tensors are shown within the 'Lumley triangle' in Fig. 2(d), from which it can be seen that the anisotropy invariants computed in this study are very similar to those reported by Vartdal[47].

It should be noted that the structure tensors obtained from half-channel flow simulations described in Sec. IV do not collapse far from the wall with those that would be obtained from full-channel simulations. This is due to the symmetry boundary condition imposed for the velocity fields and the boundary conditions for ψ_i imposed by Eqs. (3)-(5) (e.g. $\psi_2 = 0$ at $y = \delta$), which do not hold for a full channel. Detailed comparison is given in the Appendix. However, the difference between the structure tensors obtained from a half channel versus a full channel is limited to the region of $y > \delta/2$, while the effect of the rough wall is later shown to be limited to the near-wall region. Therefore, a half-channel configuration is considered herein as an efficient and effective way to demonstrate the rough-wall effect on the structure tensors.

To test the implementation of the immersed boundary method in the stream vector solver, a two-dimensional laminar tilted-channel is used. The channel is tilted in the (x, y) plane at an angle of 45° from the global coordinates of the Cartesian grid. A uniform grid is used in all directions. Here, ψ_i is obtained from analytically deduced velocity distributions, instead of velocities from a simulation with the IBM, to eliminate the error from IBM in the Navier-Stokes solver. In Fig. 3(c), results for ψ_i using the immersed boundary implementation of the ψ_i solver are compared with their counterparts obtained for flow in the same channel aligned with these coordinates, without immersed boundaries. The contour of the only non-zero component ψ_3 is shown in Fig. 3(a) across the immersed boundary. The velocities, reconstructed from ψ_i using central differencing, are compared in Fig. 3(d), after transformation to reorient ψ_i and u_i to the coordinates of the channel. A very good collapse is obtained for all ψ_i and u_i components. Figure 3(b) shows

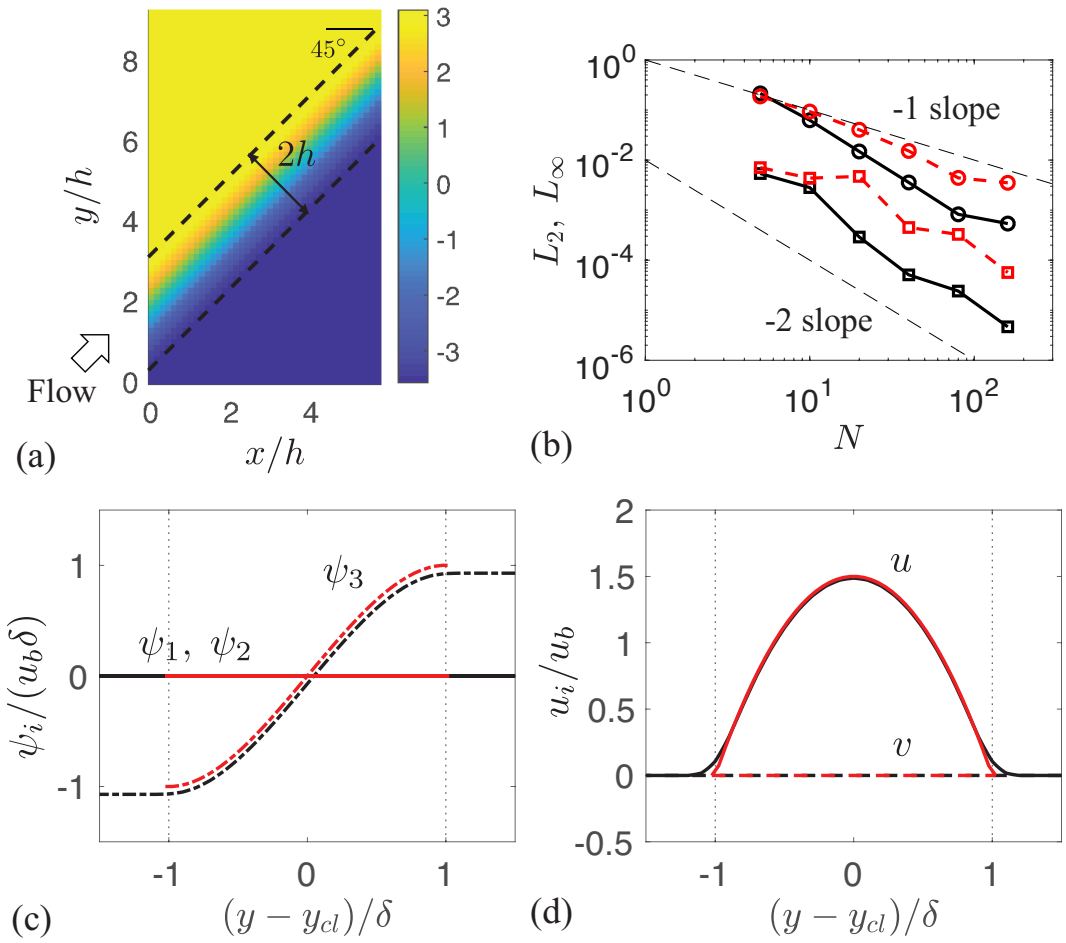

FIG. 3. Validation of the stream vector solver with immersed boundaries using a tilted laminar channel. (a) Distribution of ψ_3. (b) L_2-norm (——) and L_∞-norm (- - -) errors of reconstructed u (◯) and v (□) versus the number of grid points spanning channel height N. Comparison of (c) ψ_i and (d) reconstructed u_i for $N = 10$ between calculations with (black) and without immersed boundaries (red or dark gray). Here y_{cl} is the center-line elevation.

the L_2-norm errors of the reconstructed u and v velocities, which both decrease with increasing number of grid points across the channel at a second-order rate, while the L_∞-norm errors decrease at a rate between first and second orders. The current immersed boundary treatment of the ψ_i solver is analogous to reconstructing the immersed boundary as a stepwise geometry[48]. Such an idealization leads to local errors in the vicinity of the immersed boundary, which presumably cause the L_∞-norm error to be lower than second order. In this study, these errors are expected to be small because the wall waviness is well resolved.

The tilted channel is a simple test case since the immersed boundary is flat. To perform an error

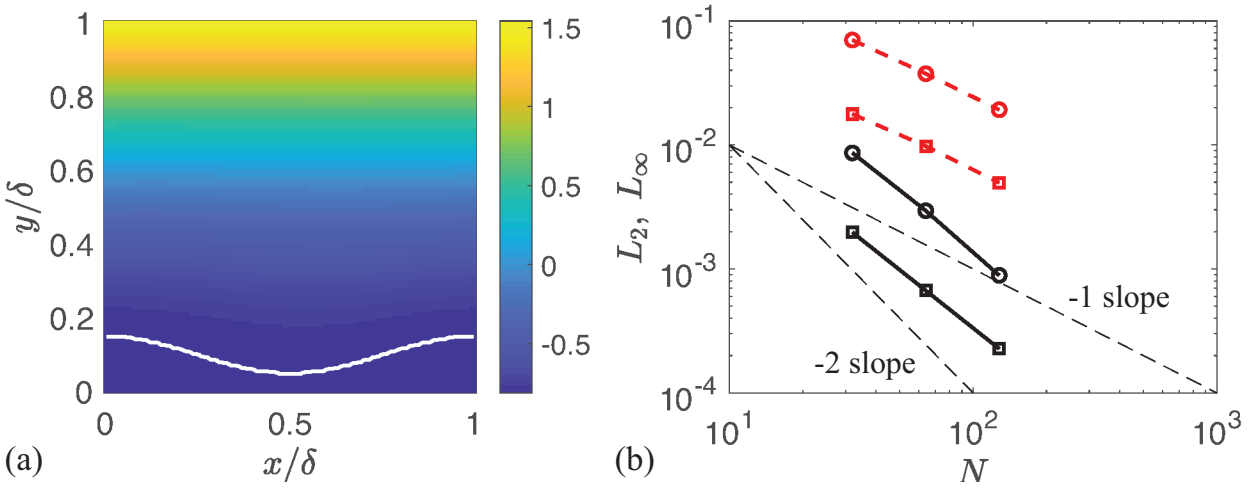

FIG. 4. Validation of the stream vector solver with an immersed boundary using a laminar channel flow with a wavy wall. (a) Distribution of ψ_3^+. White line: solid-fluid interface. (b) L_2-norm (——) and L_∞-norm (- - -) errors of reconstructed u^+ (◯) and v^+ (□) as compared with the actual u^+ and v^+ versus the number of grid points.

analysis near a curved wall, a laminar channel flow with $Re_\tau = 10$ on a wavy wall with $2a/\lambda = 0.1$, $\lambda/\delta = 1$ (larger λ than that used in the turbulent flow simulations herein) and a x domain size of 1λ is used. Uniform grids are used in both x and y. Simulations are conducted with three spatial resolutions: $n_i \times n_j = 32^2$, 64^2, and 128^2. The velocities reconstructed from ψ_i are compared to the actual velocity obtained from the simulations. Figure 4(a) displays the contour of the only non-zero component of stream vector, ψ_3, for the case with a resolution of 128^2 grid points in x and y. Figure 4(b) shows the order-of-accuracy of reconstructed u and v. The L_∞-norm errors are both first-order, while the L_2-norm errors are almost second order.

IV. RESULTS

A. The wavy-wall channel

To validate the present wavy-wall DNS simulation using the immersed boundary method, we compare the pressure-drag coefficient with existing studies using experiments or simulations with body-fitted mesh. The pressure-drag coefficient is determined by integrating the average pressure

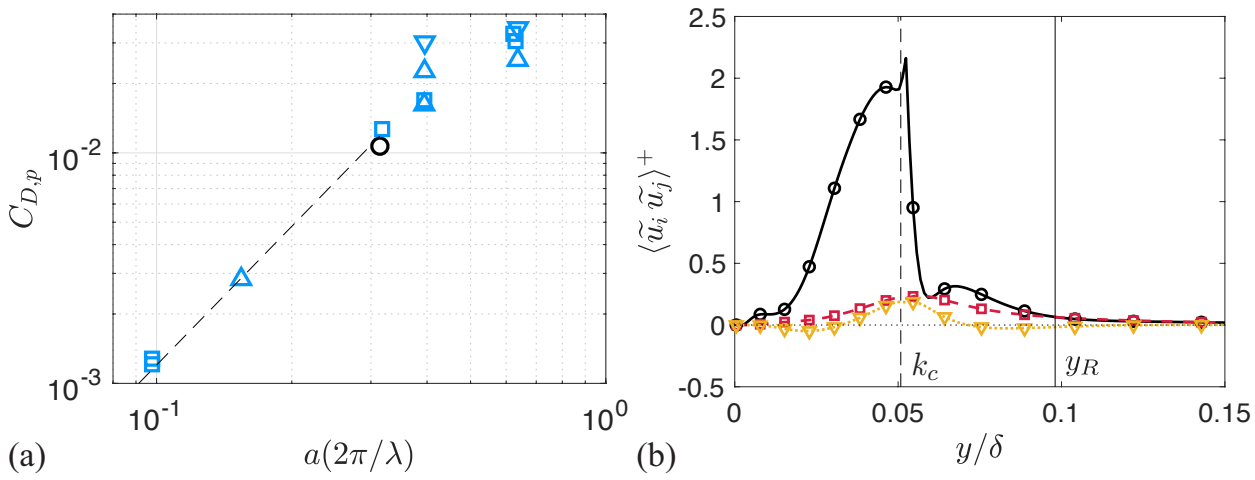

FIG. 5. (a) Wavy-channel pressure drag coefficient comparison with existing studies: ◯ present DNS, □ Henn and Sykes[37], △ Zilker and Hanratty[30], ▽ Buckles, Hanratty, and Adrian[31], - - - fitted quadratic relation[49]; (b) dispersive stresses in the wavy-wall case showing the extent of roughness sublayer, y_R. Dispersive stress components: 11 (◯), 22 (□), 12 (▽).

along the fluid-solid interface (Zilker and Hanratty[30]) as

$$C_{D,p} = \frac{1}{(1/2)\rho u_b^2 \lambda} \int_0^\lambda \overline{P} \frac{dy}{dx} dx, \tag{11}$$

where u_b is the bulk velocity. In Fig. 5, the present value is compared with the values determined experimentally by Zilker and Hanratty[30] with $Re_b \approx 14,000 - 30,000$ and $2a/\lambda = 0.05 - 0.2$ and by Buckles, Hanratty, and Adrian[31] with $Re_b \approx 10,700 - 30,000$ and $2a/\lambda = 0.125 - 0.2$. Large-eddy simulations of Henn and Sykes[37] with $Re_b = 57,00 - 10,800$ and $2a/\lambda = 0.03 - 0.2$ are also compared. These parameters bound the corresponding values of Re_b and wave slope in the present DNS. As pointed out by Henn and Sykes[37], for $a(2\pi/\lambda) \leq 0.31$, $C_{D,p}$ appears insensitive to the Reynolds number variation in this range and the prediction of $C_{D,p} \sim (2\pi a/\lambda)^2$ from the analytical model for small-amplitude waves[49] is consistent with these values. The pressure drag coefficient computed from the present DNS is in very good agreement with reference values, indicating that modifications of near-wall turbulent structure associated with the mean-flow separation and reattachment are captured accurately by the immersed boundary method of Yuan and Piomelli[25].

The roughness sublayer is defined here as the entire layer within which the streamwise dispersive stress is not negligible, i.e. $\langle \widetilde{u}^2 \rangle^{1/2} \geq 0.03 \langle \overline{u} \rangle$, which is similar to the definition used by Pokrajac *et al.*[50]. Figure 5(b) shows the distribution of the dispersive stresses and both the wave

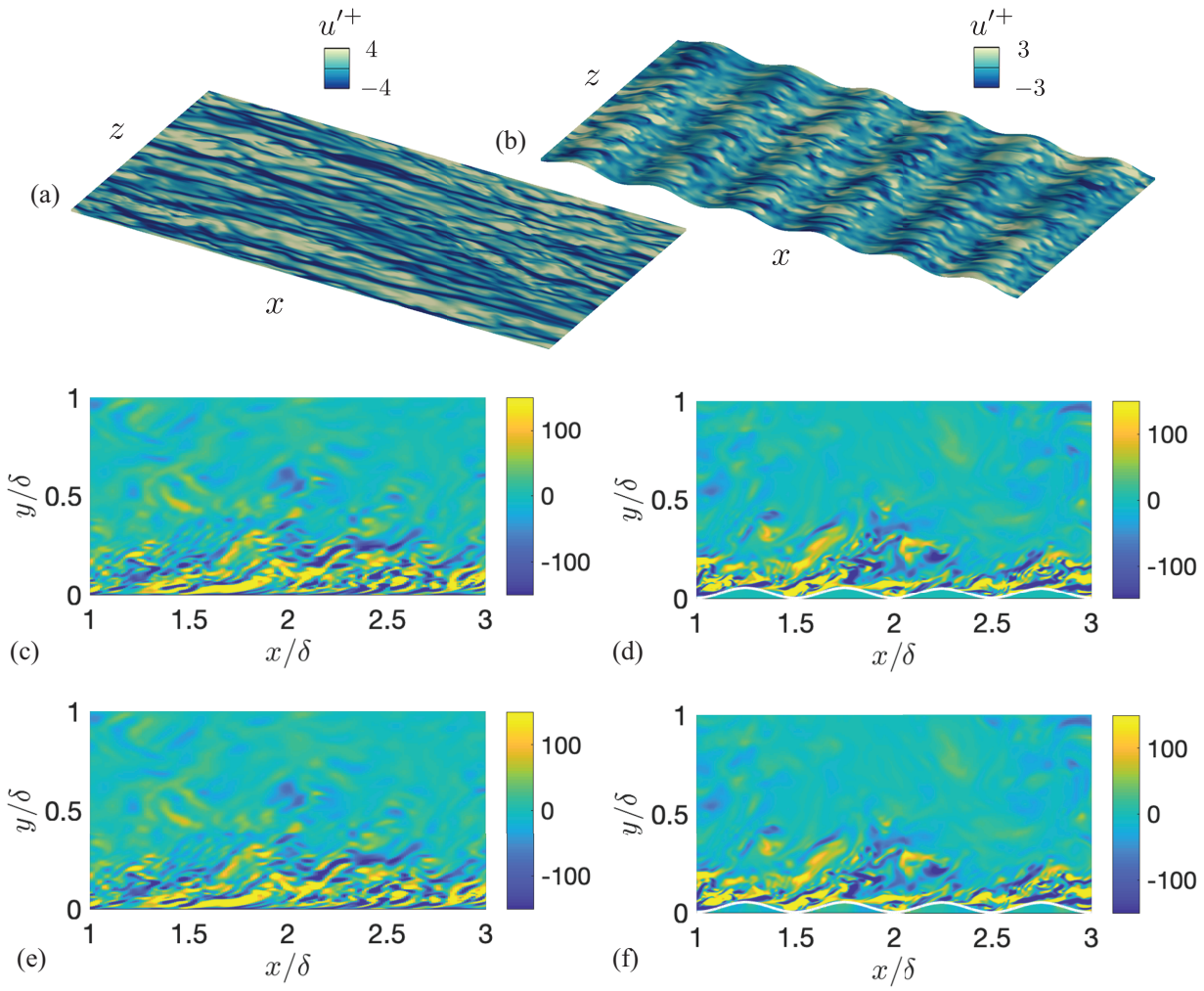

FIG. 6. Instantaneous contours of u'^+ at an elevation of 13 wall units above the wall in 1/4 of the x-z domain (a,b), contours of ω_z^+ of the original DNS velocity (c-d), and ω_z^+ reconstructed from ψ_i (e-d) in the wall-normal plane at $z/\delta = 1.5$, on the smooth wall (a,c,e) and the wavy wall (b,d,f). Solid while lines indicate immersed boundaries. Flow goes from left to right.

crest height k_c and the border of the roughness sublayer y_R in the wavy-wall case. The sublayer is confined mostly to the region $y/\delta \lesssim 0.1$. As will be shown later, this layer contains the majority of the effects of wall waviness on the structure tensor components.

Figure 6(a,b) compares instantaneous values of u'^+ at an elevation of 13 wall units away from the wall, which corresponds to the buffer layer above the smooth wall, and in the roughness sublayer in the wavy-wall case. This elevation was chosen to allow a comparison of the representative near-wall characteristics in the two flows. Farther away from the wall toward the edge of the roughness sublayer, the velocity contours become increasingly similar in the two cases (not shown). A

clear structural change is evident, which is associated with the break-up of low-speed streaks. De Angelis et al.[32] also suggested that the streaks appear to be generated at the reattachment point and to be extinguished at the next reattachment point with a new cycle starting, based on the ratio of local u' production and dissipation. It will be shown in Section IV B that the single-point structure tensors capture the shortened streaky motions. Figure 6(c-f) compares the instantaneous distributions of ω_z^+ in an (x,y) plane obtained using the original DNS velocity data and the vorticity reconstructed from ψ_i, for both cases. It can be seen that the reconstructed fields match the original fields very well, with or without the immersed fluid-solid boundary.

B. Comparison of structure tensors over smooth and wavy walls

The structure tensors for flow over smooth and wavy-wall boundaries are compared in Fig. 7 and 8 using logarithmic and linear scales, respectively. The components of the Inhomogeneity tensor are normalized by wall units, to compare the relative inhomogeneity between different locations and between cases. For the other tensors, the self-normalized form in Eq. (8) is used to show differences in their anisotropies.

The Inhomogeneity tensor C_{ij} (plotted as its symmetric equivalent $C_{ij}+C_{ji}$) is shown in Fig. 7(a). The extent of the wall layer within which turbulence has significant inhomogeneity is important for modeling purposes as, beyond this layer, the state of homogeneous turbulence can be specified fully by only two structure tensors[6]. Above the smooth wall, the inhomogeneous region (with non-negligible $C_{ij}+C_{ji}$) extends to $y^+ \approx 30$ whereas, over the wavy wall, the inhomogeneous region is confined to the roughness sublayer on account of the roughness-scale form-induced shear $\partial\widetilde{u}_i/\partial x_j$ there. A small peak is visible for the C_{22} component at around k_c. This is perhaps due to the significant spatial variation of $\partial\widetilde{u}_i/\partial y$ associated with the thin attached local mean shear layers on the peak of the sinusoidal wall and above the mean recirculation regions.

In general, waviness increases the near-wall isotropy of r_{ij}, d_{ij}, and f_{ij}, as well as the magnitudes of their off-diagonal components. For r_{ij}, this observation is consistent with the findings of Smalley *et al.*[51], Busse and Sandham[52] and Flack and Schultz[53].

The normalized Circulicity tensor f_{ij} is plotted in Fig. 7(d). The dominance of the 22 and 33 components of f_{ij} near the smooth wall is due to $\partial u'/\partial y$ and $\partial u'/\partial z$ on account of low- and high-speed streaks[45]. Furthermore, the rapid increase of the 11 component with increasing distance from the smooth wall toward a peak at $y^+ \approx 30$ is a consequence of the quasi-streamwise vortices

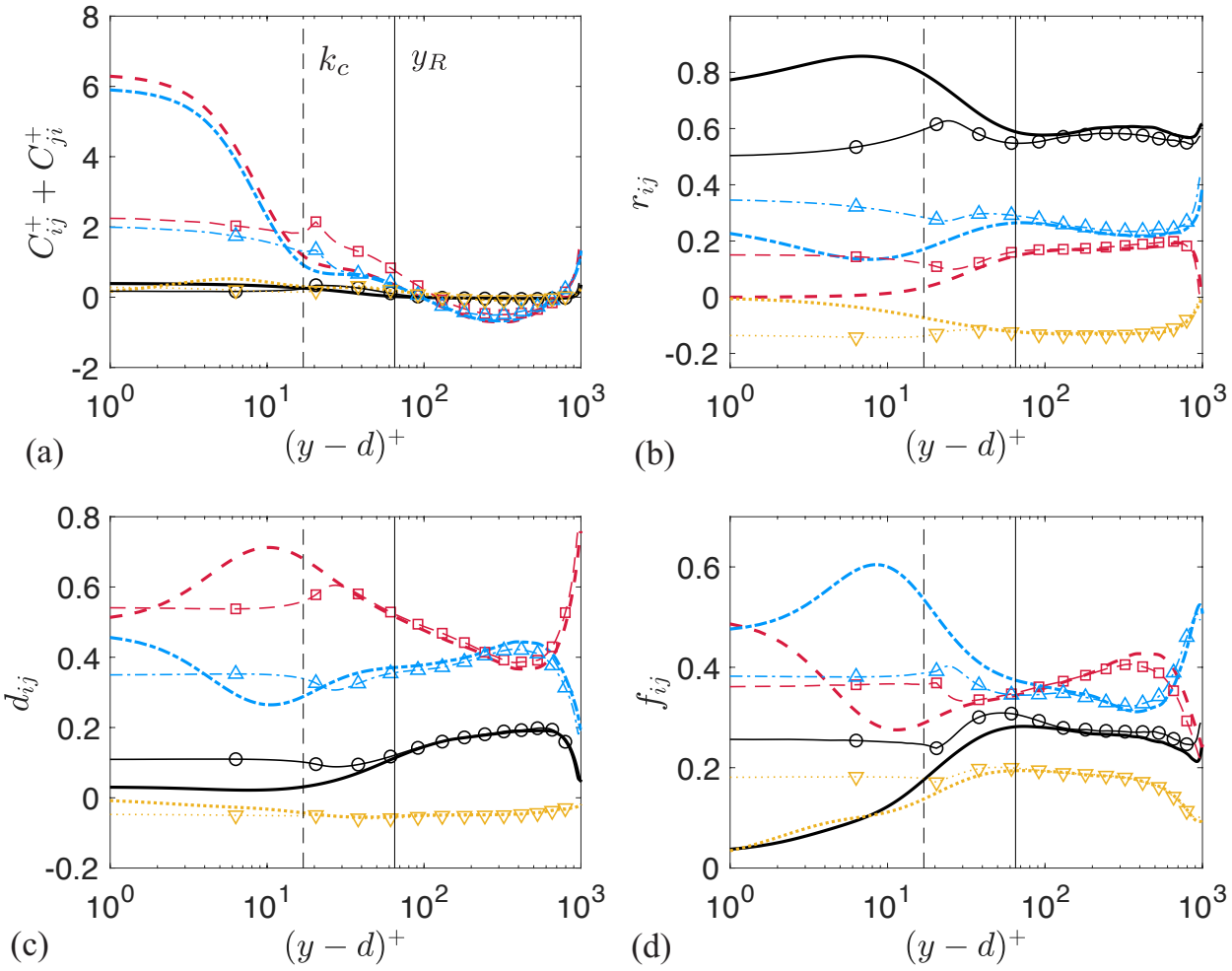

FIG. 7. Inhomogeneity tensor (a) and normalized Reynolds-stress (b), Dimensionality (c) and Circulicity tensors (d) along y in logarithmic scale. Smooth-wall components: 11 (——), 22 (- - -), 33 (-- -), 12 (- - -). Lines with symbols show Wavy-wall components: 11 (◯), 22 (□), 33 (△), 12 (▽). In the smooth case $(y-d)^+$ reduces to y^+.

in this region. On the wavy wall, all diagonal components remain significant in the vicinity of the wall, consistent with the presence of roughness-scale three-dimensional vortical structures in the sublayer of a fully rough flow, such as the head-down and head-up hairpins[54]. Orlandi and Leonardi[55] also observed greater isotropy in the vorticity near rough walls than near smooth ones.

Lastly, the normalized Dimensionality tensor d_{ij} is plotted in Fig. 7(c). For this structure tensor, higher values of diagonal components represent shorter coherence in the corresponding direction. From the figure, it can be seen that, in the roughness sublayer, waviness weakens the streamwise elongation of structures by enhancing d_{11}, while driving d_{22} and d_{33} closer to equality (similar

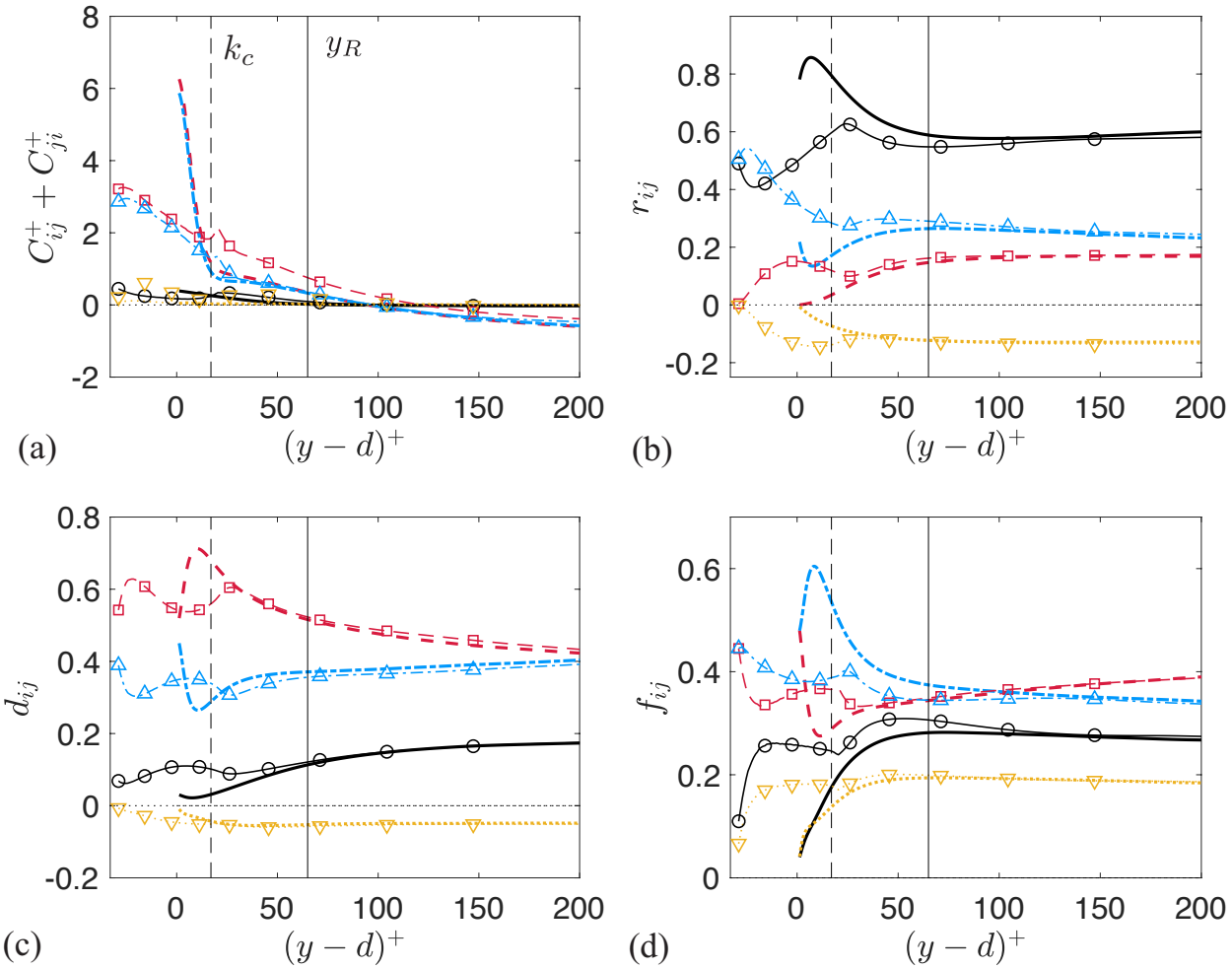

FIG. 8. Inhomogeneity tensor (a) and normalized Reynolds-stress (b), Dimensionality (c) and Circulicity tensors (d) along y in linear scale. For legends see Fig. 7.

coherence in z and y) as the waviness imposes its scales on the flow. The deductions from this single-point tensor comparison are consistent with the instantaneous picture of turbulence in Fig. 6.

We also note that Townsend's similarity hypothesis seems to apply not only to turbulence componentality, but also to Dimensionality and Circulicity. Although discernible differences between the smooth- and wavy-wall flows are observed in the outer layer for f_{ij} in Fig. 7(d), these differences are no more than 3% of their trace values.

To show the spatial variation of various tensors, the (x, y) contours of R_{ij}^+, D_{ij}^+ and F_{ij}^+ obtained using statistics of ψ_i' gradients averaged in time and z (instead of time and both x and z as shown in Fig. 7) are displayed in Fig. 9. The dividing streamline is obtained as the contour line of $\overline{\Psi}_3$ value at the immersed boundary; it quantifies the extend of the separation bubble. The variations

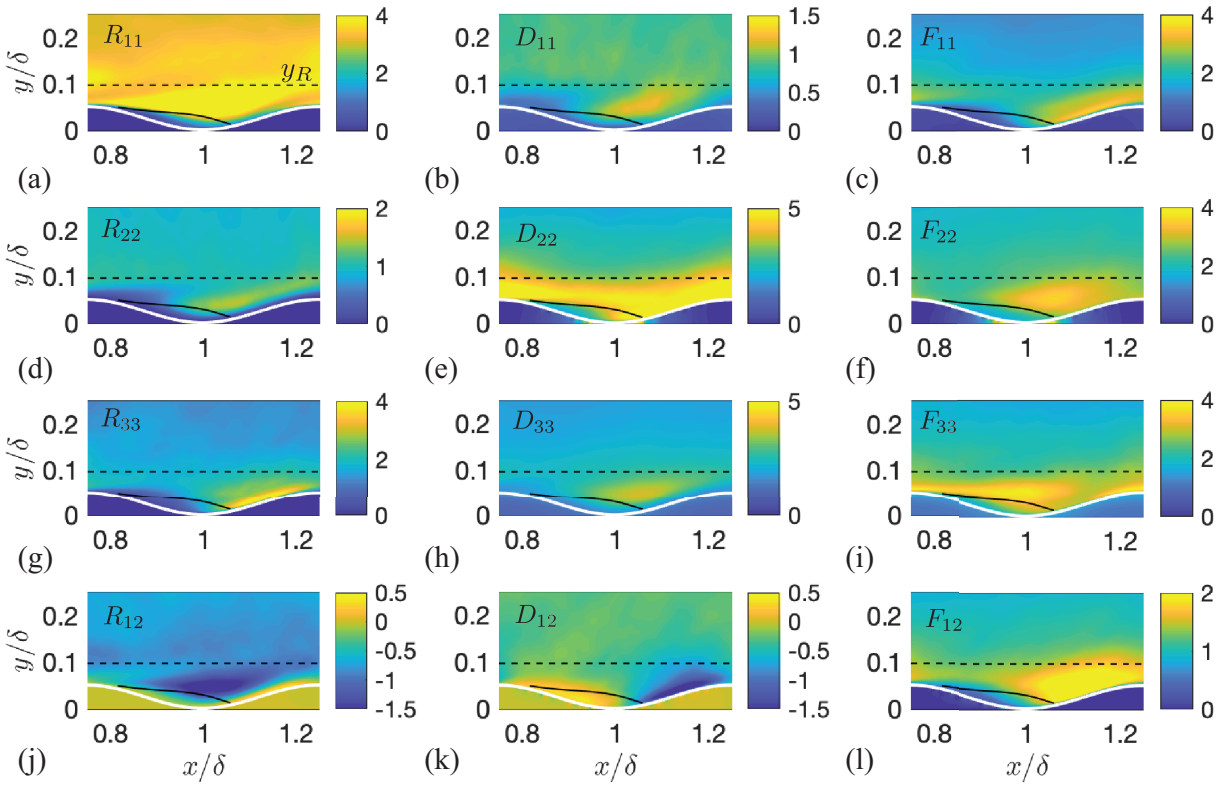

FIG. 9. Contour of 11 (a-c), 22 (d-f), 33 (g-i) and 12 components (j-l) of R_{ij}^+ (a,d,g,j), D_{ij}^+ (b,e,h,k), F_{ij}^+ (c,f,i,l) tensors. White lines indicate solid-fluid interface. Black lines: top of the roughness sublayer (- - -) and dividing streamline (———).

of R_{ij} components shown in Fig. 9(a,d,g,j) match very well with results available in the literature (for example, see experimental measurements of Hudson et al.[8]). The dominant dynamical phenomena include the following. (i) The detached shear layer corresponding to the $\overline{u}$ inflection point significantly augments the Reynolds shear stress and u' production. (ii) A thin boundary layer is generated at the reattachment point, where significant TKE redistribution takes place, mostly from u' to w' energy. (iii) Flow acceleration on the upslope side leads to increased u' and v' due to productions associated with more intense $\partial\overline{u}/\partial x$ and $\partial\overline{v}/\partial x$, respectively. (iv) Below the separated shear layer, a retarded flow region is formed where the Reynolds stresses are relatively weak and the TKE is maintained by but diffusion processes, instead of production. Comparing the middle of the roughness sublayer (e.g. $y \approx d$) in the wavy-wall case and the buffer layer (e.g. $y^+ = 10$) on the smooth wall, the aforementioned phenomena lead to weaker r_{11} and stronger r_{22}, r_{33} and r_{12} components on the wavy wall. For the Dimensionality tensor, Fig. 9(b,e,h) show that inside the detached shear layer the coherent motions are shortened in all directions in an average sense, most

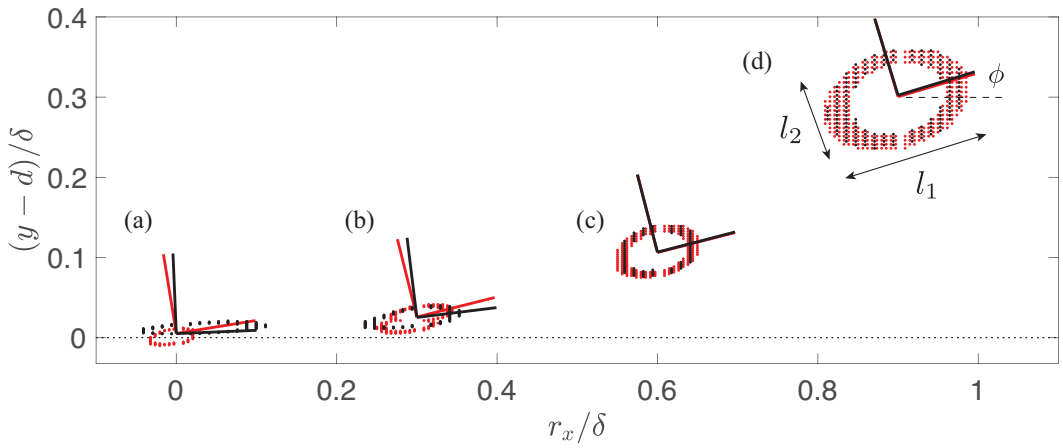

FIG. 10. Contour of the trace of the two-point velocity correlation tensor, $\mathscr{R}_{kk}(r_x, r_y)$ at a contour level between 0.7 and 0.8 centered at $y-d = 5\delta_v$ (a), $25\delta_v$ (b), 0.1δ (c), and 0.3δ (d). Black: smooth case; red (or dark gray): rough case. Short lines indicate axes of the isocontours. Contours are shifted in r_x by 0.3 units for clarity.

significantly for the x and z extents. This is probably due to the production of smaller-scale new turbulence inside the shear layer. The result is a more isotropic D_{ij} tensor near the wall. Fig. 9(f) shows that F_{33} decreases as the reattachment point is approached, perhaps due to the breakup of streaky motions (and consequently weaker $\partial u'/\partial y$) as three-dimensional vortical motions are generated as a result of shear layer roll-up. These vortical motions also lead to augmented F_{22} in the detached shear layer. In addition, F_{11} appears to increase in the thin boundary layer generated after reattachment, probably connected to the higher turbulence production resulting in stronger streamwise vorticity fluctuations. Such damping of F_{33} and augmentation of F_{22} near the reattachment point, as well as the increase of F_{11} in the thin shear layer, lead to an overall more isotropic Circulicity tensor near the wall as observed in Fig. 7.

C. Connection between the Dimensionality tensor and the two-point velocity correlation

For homogeneous turbulent flows, Bhattacharya, Kassinos, and Moser [7] showed that the eigenvalue ratio and principal-axis inclinations of D_{ij} correspond respectively to the aspect ratio and

inclination of the isocontour of the trace of two-point velocity correlation tensor

$$\mathscr{R}_{\alpha\beta}(r_i) = \langle \overline{u'_\alpha(x_i,t)u'_\beta(x_i+r_i,t)} \rangle / \langle \overline{u'_\alpha u'_\beta} \rangle, \tag{12}$$

where $\vec{r} = r_x\vec{i} + r_y\vec{j}$ is the separation between the two points. For such a connection to be valid, the $\vec{r}$ magnitude must be within the inertial subrange.

We now test whether this homogeneous-flow correspondence applies to inhomogeneous turbulence at low local Reynolds numbers in the near-wall region, taking care to calculate $\mathscr{R}_{\alpha\beta}(r_i)$ only where there is no contribution from within the solid. Values of $\mathscr{R}_{kk}$ ranging from 0.55 to 0.85 are used to show the trend and the level of uncertainty in this two-point correlation. Within this $\mathscr{R}_{kk}$ range, all isocontours satisfy $|\vec{r}|^+ > 10$ and so exclude contributions from the dissipative subrange. In addition, $|\vec{r}|/\mathscr{L} \lesssim 0.25$, where $\mathscr{L}$ is the x extent of the isocontour of $\mathscr{R}_{kk} = 0.3$ at each y-location, which is considered to be a measure of the largest scale of the coherent motion. Thus, the upper cut-off value of $|\vec{r}|$ used here largely (though not completely) excludes the contribution from the integral scales.

Figure 10 compares the evolution of the $\mathscr{R}_{kk}(r_x, r_y)$ isocontour along y. The isocontours are identified using $\mathscr{R}_{kk}$ values between 0.7 and 0.8 for demonstration purposes, though using another contour value range does not alter the evolutionary trend. The isocontour axes are identified using principal component analysis. At each y location, the inclination and shape of the isocontour is characterized by: (1) the inclination angle ϕ of the isocontour axis with respect to the (x,y) coordinate; and (2) the aspect ratio (AR), l_1/l_2, where l_1 is the isocontour length along the principal component and l_2 is the length in the orthogonal direction.

In Fig. 11, a comparison is made between the values of ϕ and l_1/l_2 obtained from $\mathscr{R}_{kk}$ isocontours and their corresponding D_{ij}-tensor representations. Far from the wall, the tensor representations are very close to the true structural properties (with allowance for scatter in the data) for both smooth- and wavy-wall flows. A good collapse might be expected as the relatively high local Reynolds number results in an inertial subrange of significant extent and the flow is locally homogeneous. Near the wall, waviness leads to a clear increase in the inclination angle and a reduction in the aspect ratio. The tensor representations capture both near-wall changes qualitatively but not quantitatively according to the relations identified by Bhattacharya, Kassinos, and Moser[7]—possibly because the assumptions of a prominent inertial subrange and homogeneous turbulence do not apply near the wall. The inclusion of information from the Inhomogeneity tensor in a structure-tensor-based model of $\mathscr{R}_{ij}$ characteristics might result in better agreement near

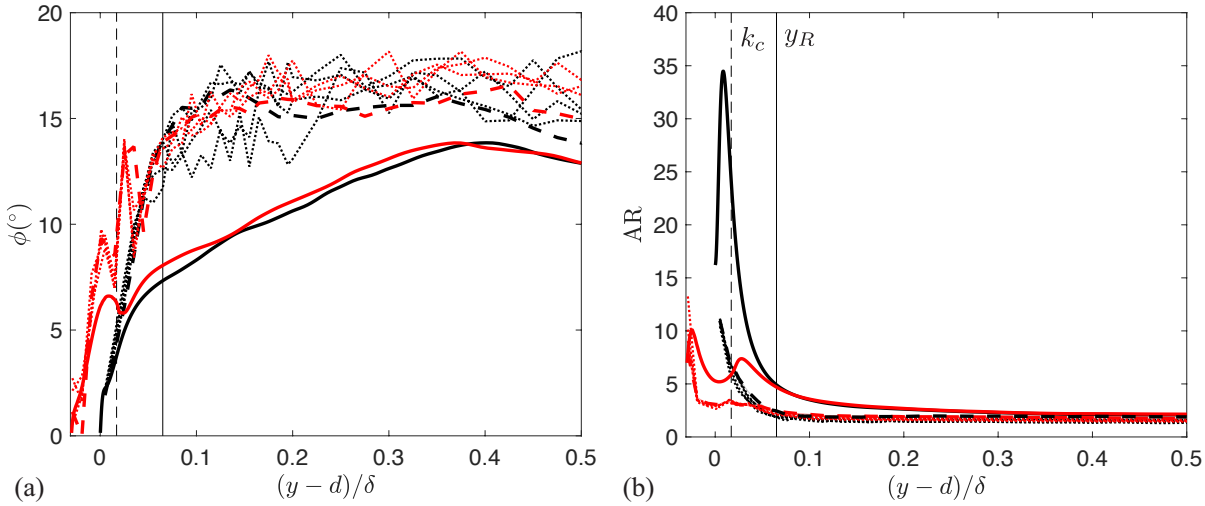

FIG. 11. Properties of the true structure (– – –) and its tensor prediction (——) in smooth (black) and rough (red or dark gray) cases using $\mathscr{R}_{kk}$ range of 0.55-0.65: (a) inclination angle and (b) aspect ratio (AR) of $\mathscr{R}_{kk}$ isocontour. - - - Tensor predictions from $\mathscr{R}_{kk}$ ranges of 0.6-0.7, 0.65-0.75 and 0.75-0.85.

the wall—a topic to be explored in future work.

D. Principal tensor information

For structure-based closures such as that of Kassinos and Reynolds[5], it is impractical to impose boundary conditions on each tensor component. Instead, one imposes the minimum amount of information required to describe the structural change between the wall and the outer layer, both for smooth and wavy walls. One approach is to decompose a full tensor into: (1) the principal-axis inclination angle; and (2) a measure of tensor anisotropy which, together with the tensor trace, describe the principal information of the tensor.

In Fig. 12(a), the principal-axis inclination angle is shown for each tensor. For the smooth case, the inner-layer ($y/\delta < 0.1$) distributions are very similar to the smooth-wall pipe-flow results obtained by Stylianou, Pecnik, and Kassinos[45] at $Re_\tau \approx 180$. Waviness results in significantly higher inclination angles near the wall, comparable to their values at the edge of the roughness sublayer.

The tensor anisotropies may be characterized on a barycentric map[56], which is designed to present visually the state of turbulence in an equilateral triangle which weights equally the differ-

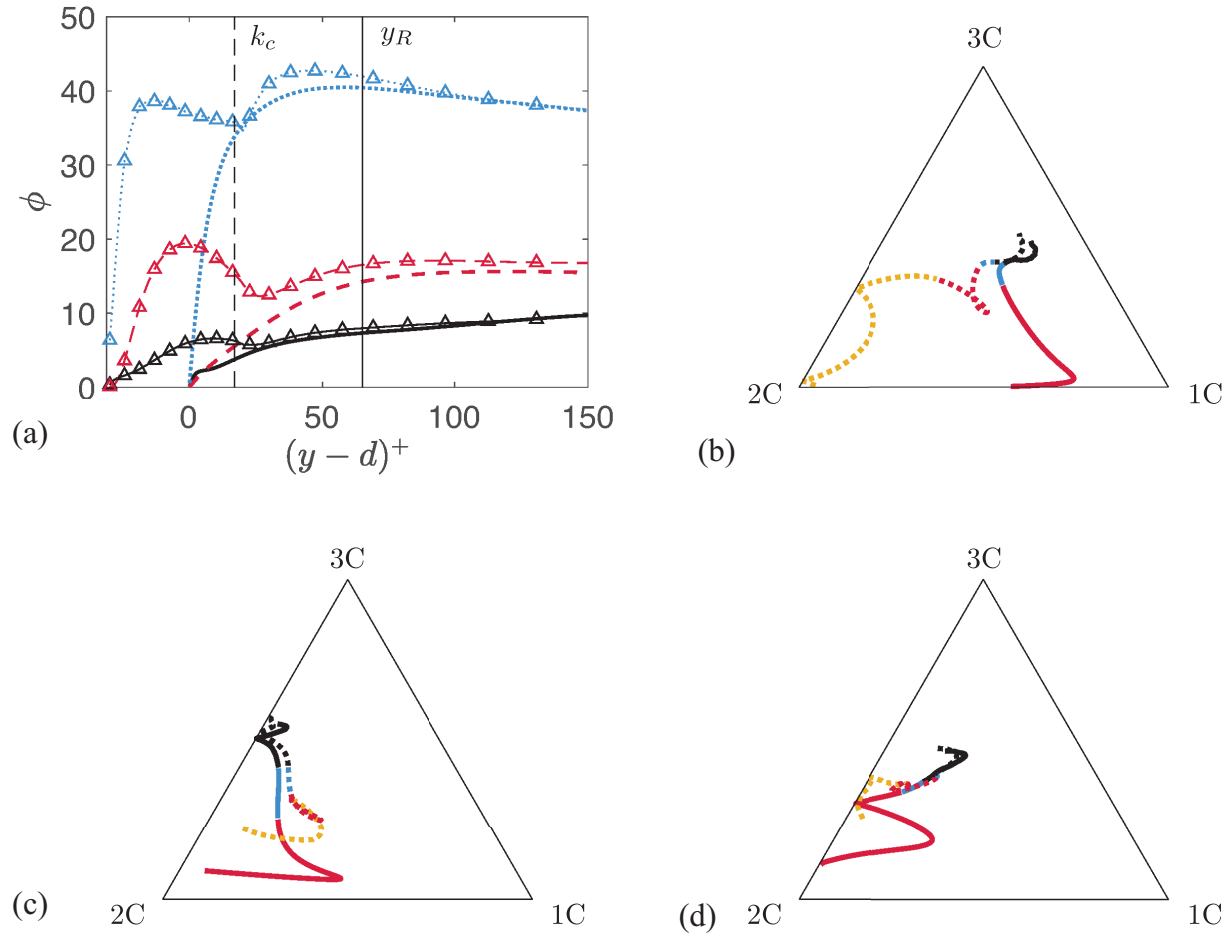

FIG. 12. (a) Inclination angles (in degrees) of principal axes of D_{ij} (——), R_{ij} (- - -) and F_{ij} (- - -) tensors for smooth wall (lines) and wavy wall (△) cases. Barycentric maps showing the change of anisotropies of R_{ij} (b), D_{ij} (c), and F_{ij} (d) tensors for smooth wall (——) and wavy wall (- - -) cases. ——, - - -: $0.1\delta \leq y \leq 0.6\delta$; ——, - - -: overlap region, $50\delta_v \leq y \leq 0.1\delta$ for smooth wall flow and $y_R \leq y \leq 0.1\delta$ for wavy wall flow; ——: viscous wall region ($y \leq 50\delta_v$) for smooth wall flow; - - - ($d \leq y \leq y_R$) and - - - ($y \leq d$): roughness sublayer for wavy wall flow.

ent limiting states. The one-component (1C) state describes the flow where the tensor-represented properties (fluctuations, spatial variations, or large scale circulation) exist only in one direction. The axisymmetric two-component (2C) state describes turbulence where these properties exist along two directions with equal magnitude, and the isotropic (or three-component 3C) state describes flow where the properties are of equal strength in all directions.

The tensor anisotropies are shown on barycentric maps in Fig. 12(b-d). In Fig. 12(b) it may be

seen that on a smooth wall R_{ij} develops from the two-component limit in the buffer layer, where much of its turbulence kinetic energy (TKE) is in the u' component and associated with the low-speed streaks, to a state much closer to 3C in and above the overlap region where $y^+ > 50$. In Fig. 12(c), it can be seen that D_{ij} also transitions from close to the two-component limit at the wall (due to very long coherence in the x direction with $D_{11} \approx 0$) to an axisymmetric state with one small eigenvalue far from the wall, with structure elongation predominantly in the x direction and correspondingly weaker in y and z directions, with $D_{22} \approx D_{33} > D_{11}$. In Fig. 12(d), it can be seen that very near the wall F_{ij} is near the axisymmetric two-component state because the flow is dominated by circulation around the y and z axes, as a consequence of low and high velocity streaks. F_{ij} then changes towards the 3C state with increasing distance from the wall.

For flow over the wavy-wall, it is evident that the tensor anisotropy above the roughness sublayer follows closely the variation in the smooth case. In the upper part of the roughness sublayer above the virtual wavy-wall origin ($y > d$), all three structure tensors are at a state close to that in the overlap region. This is presumably because, inside the roughness sublayer, quasi-streamwise vortices coexist with smaller-scale eddies generated by mechanisms such as shear-layer roll-up[57] near local wake regions (see, for examples, Martinuzzi and Tropea[58] and Talapatra and Katz[54]). In contrast, a significant departure from the buffer-layer state is observed below the virtual origin ($y < d$), especially for R_{ij}, which takes the shape of an oblate spheroid other than the prolate one observed in smooth-wall flow. Busse and Sandham[52] also observed this behavior in R_{ij} in the lower part of the sublayer adjacent to a random synthetic wall roughness, and attributed it to stronger damping of u' motions than v' and w' motions in this layer. Below the virtual wavy-wall origin, D_{ij} is more isotropic than in their respective buffer-layer states, where a weaker structure elongation in the x direction yields values of D_{ij} further from the two-component limit. Also, F_{ij} is further from the 2-component axisymmetric limit in the lower portion of the roughness sublayer than in the buffer layer, as a result of more significant x-axis circulation caused by three-dimensional vortices there. From the perspective of turbulence model closure, the upper portion ($y > d$) of the roughness sublayer of the wavy (fully rough) flow appears to be structurally similar to the outer layer, in the Componentality, Dimensionality and Circulicity of its turbulence.

The observation of greater isotropy in turbulence statistics within the roughness sublayer has important implications for modeling of wavy- and rough-wall flows. For example, in smooth-wall flows, the sharp near-wall peaks in quantities such as $\langle\overline{u'^2}\rangle$ and TKE require wall functions in Reynolds-averaged Navier-Stokes closures and render model equations so stiff that smoothing

approaches such as elliptic relaxation[59] are often needed to satisfy boundary conditions. However, in wavy- and rough-wall flows, the degree of turbulence anisotropy is greatly reduced within the roughness sublayer. This observation implies that, although the specification of precise boundary conditions at a virtual origin may not be straightforward, the modeling of a more isotropic turbulence may be simpler and may not require such stiff model equations or relaxation techniques to accommodate boundary conditions. This observation is supported by the modeling studies of Brereton and Yuan[60], who show that the dominant contribution to shear stress in the roughness sublayer in turbulent flows in rough-wall channels comes from the viscous and pressure forces over roughness elements, which can be modeled as an eddy viscosity or an effective local body force. The dominance of this term over the Reynolds and dispersive stresses in the roughness sublayer lessens some of the limitations of Reynolds-stress closures when applied in smooth-wall flows.

V. CONCLUSIONS

An overarching objective of many turbulence modeling efforts is to improve the fidelity of closures by integrating a higher degree of underlying physics within the closure model. To this end, a promising approach is to append to the modeling basis by adding tensors that carry information regarding features of turbulence physics that are difficult to represent in existing models. In this context, single-point turbulence structure tensors appear to be very promising as they are effective measures of non-local characteristics of homogeneous turbulence[5]. While the capability of such tensors to improve model fidelity has been verified for homogeneous turbulence, in this work, we show that for complex inhomogeneous turbulence, these tensors also contain qualitative information on the computed turbulence structure, which we quantify throughout the flow over a wavy wall. An immersed-boundary approach for solving the vector Poisson equation is adopted to solve for the stream vector to extract these tensors on an ideal (wavy), two-dimensional rough surface and can potentially be used for establishing databases of single-point structure tensors for structure-based model development for more complex wall-roughness geometries.

DNS results show that, in the sublayer adjacent to the rough/wavy surface, turbulence is inhomogeneous. In this sublayer, the Dimensionality structure tensor describes qualitatively higher-order effects such as the near-wall structure inclination angle on account of waviness, as well as the shortening of streamwise coherence lengths of turbulence motions. Furthermore, the Circulicity

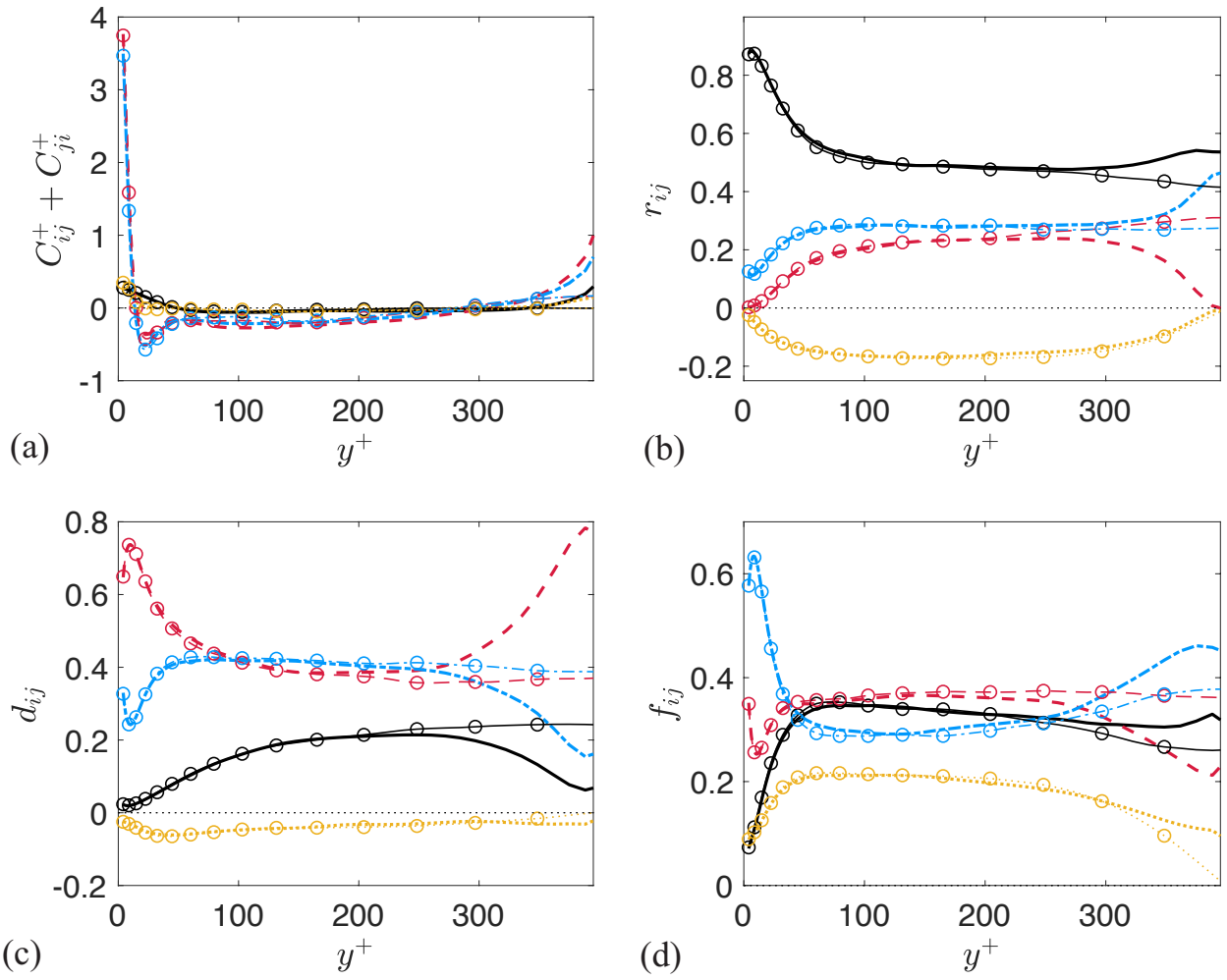

FIG. 13. Comparison of Inhomogeneity tensors (a) and normalized Reynolds-stress (b), Dimensionality (c) and Circulicity tensors (d) obtained from a full channel (lines with symbols) and half channel (lines only), both with a smooth wall and $Re_\tau = 395$. Components: 11 (——), 22 (– – –), 33 (–· –), 12 (···).

tensor becomes more isotropic in the sublayer, consistent with the emergence of roughness-scale eddies. Beyond the roughness sublayer, Townsend's similarity hypothesis appears to apply not only to the componentality of turbulence, but also to its Dimensionality and Circulicity. Even within the roughness sublayer above the virtual origin, turbulence above a wavy or rough surface appears to be structurally simpler compared with a smooth-wall flow. This is encouraging from a modeling standpoint. In general, tensor characteristics such as principal-axis inclination and anisotropy are shown to be sensitive to both the presence of wall waviness and the distance from the surface. Thus structure-tensor characteristics may also prove to be useful for imposing wall boundary conditions for use with structure-based turbulence models.

ACKNOWLEDGMENTS

The authors gratefully acknowledge the support of Stanford University's Center for Turbulence Research and the inspiration of W. C. Reynolds. J.Y. and G.B. acknowledge the Office of Naval Research for the financial support of this research (Award No. N00014-17-1-2102).

Appendix: Structure tensors extracted from a half channel

The half-channel configuration is used in this work as an efficient way to explore the difference brought by roughness in a channel flow. In this section, we show the discrepancy between the results obtained from a half channel simulation and a full-channel one. Tensors extracted from the LES simulations of a full-channel flow with $Re_\tau = 395$ and those from its half-channel counterpart are compared in Fig. 13. In the region $y/\delta < 0.5$ (or $y^+ < 200$), the two cases collapse perfectly. In the region $0.5 < y/\delta \leq 1$, differences are increasingly significant as y increases. At $y/\delta = 1$, the symmetry condition for velocities gives $r_{22} = 0$, causing differences in the other two components also, since $r_{11} + r_{22} + r_{33} = 1$. The other tensors are also affected due to the identity[61],

$$R_{ij} + D_{ij} + F_{ij} - (C_{ij} + C_{ji}) = \delta_{ij} R_{kk}. \tag{A.1}$$

Furthermore, the ψ_i boundary conditions at the top boundary of a half channel do not hold for a full channel. For example, ψ_2 is set to zero at $y/\delta = 1$ according to Eq. (3) for a half channel, while for a full channel ψ_2 is free to take any value at the channel center line. Despite these differences, a half channel is considered effective in studying the roughness effect, which is shown limited to the near-wall region only.

REFERENCES

[1]J. O'Neil and C. Meneveau, "Spatial correlations in turbulence: Predictions from the multifractal formalism and comparison with experiments," Phys. Fluids A **5**, 158–172 (1993).

[2]P. Sagaut and C. Cambon, *Homogeneous turbulence dynamics*, Vol. 10 (Cambridge University Press, 2008).

[3]A. A. Mishra, G. Iaccarino, and K. Duraisamy, "Sensitivity of flow evolution on turbulence structure," Phys. Rev. Fluids **1**, 052402–1–11 (2016).

[4]A. A. Mishra, K. Duraisamy, and G. Iaccarino, "Estimating uncertainty in homogeneous turbulence evolution due to coarse-graining," Phys. Fluids **31**, 025106–1—14 (2019).

[5]S. C. Kassinos and W. C. Reynolds, "A structure-based model for the rapid distortion of homogeneous turbulence," Report TF-61 (Thermosciences Division, Department of Mechanical Engineering, Stanford University, 1994).

[6]S. C. Kassinos, W. C. Reynolds, and M. M. Rogers, "One-point turbulence structure tensors," J. Fluid Mech. **428**, 213–248 (2001).

[7]A. Bhattacharya, S. C. Kassinos, and R. D. Moser, "Representing anisotropy of two-point second-order turbulence velocity correlations using structure tensors," Phys. Fluids **20**, 101502–1—13 (2008).

[8]J. D. Hudson, L. Dykhno, and T. J. Hanratty, "Turbulence production in flow over a wavy wall," Exp. Fluids **20**, 257–265 (1996).

[9]S. Nakagawa and T. J. Hanratty, "Particle image velocimetry measurements of flow over a wavy wall," Phys. Fluids **13**, 3504–3507 (2001).

[10]E. Bou-Zeid, C. Meneveau, and M. B. Parlange, "Large-eddy simulation of neutral atmospheric boundary layer flow over heterogeneous surfaces: Blending height and effective surface roughness," Water Resour. Res. **40**, W02505 (2004).

[11]J. Finnigan, "Turbulence in plant canopies," Annu. Rev. Fluid Mech. **32**, 519–571 (2000).

[12]J. Jiménez, "Turbulent flows over rough walls," Annu. Rev. Fluid Mech. **36**, 173–196 (2004).

[13]H. Schlichting and K. Gersten, *Boundary-layer theory* (Springer, 2016).

[14]R. J. Adrian, C. D. Meinhart, and C. D. Tomkins, "Vortex organization in the outer region of the turbulent boundary layer," J. Fluid Mech. **422**, 1–54 (2000).

[15]E. K. Kalinin and G. A. Dreitser, "Heat transfer exhancement in heat exchangers," Advances in Heat Transfer **31** (1998).

[16]D. C. Wilcox, "Reassessment of the scale-determining equation for advanced turbulence models," AIAA J. **26**, 1299–1310 (1988).

[17]A. Hellsten and S. Laine, "Extension of the $k-\omega$ shear-stress transport turbulence model for rough-wall flows," AIAA J. **36**, 1728–1729 (1998).

[18]T. Knopp, B. Eisfeld, and J. B. Calvo, "A new extension for $k-\omega$ turbulence models to account for wall roughness," Int. J. Heat Fluid Flow **30**, 54–65 (2009).

[19]D. C. Wilcox, "Formulation of the $k-\omega$ turbulence model revisited," AIAA J. **46** (2008).

[20]V. C. Patel, "Perspective: flow at high Reynolds number and over rough surfaces—Achilles heel of CFD," Journal of Fluids Engineering **120**, 434—444 (1998).

[21]J. George, A. De Simone, G. Iaccarino, and J. Jimenez, "Modeling roughness effects in turbulent boundary layers by elliptic relaxation," in *Proc. Summer Program, Center for Turbulence Research* (2010) pp. 119–128.

[22]L. Wei, X. Ge, J. George, and P. Durbin, "Modeling transition on smooth and rough blades," in *ASME 2016 Fluids Engineering Division Summer Meeting collocated with the ASME 2016 Heat Transfer Summer Conference and the ASME 2016 14th International Conference on Nanochannels, Microchannels, and Minichannels* (American Society of Mechanical Engineers Digital Collection, 2016).

[23]L. Wei, X. Ge, J. George, and P. Durbin, "Modeling of laminar-turbulent transition in boundary layers and rough turbine blades," Journal of Turbomachinery **139**, 111009 (2017).

[24]J. Nikuradse, "Laws of flow in rough pipes," NACA Technical Memorandum 1292 (1933).

[25]J. Yuan and U. Piomelli, "Numerical simulations of sink-flow boundary layers over rough surfaces," Phys. Fluids **26**, 015113–1—015113–28 (2014).

[26]J. Yuan and U. Piomelli, "Roughness effects on the Reynolds stress budgets in near-wall turbulence," J. Fluid Mech. **760**, R1 (2014).

[27]A. Scotti, "Direct numerical simulation of turbulent channel flows with boundary roughened with virtual sandpaper," Phys. Fluids **18**, 031701–1—4 (2006).

[28]J. Yuan and U. Piomelli, "Estimation and prediction of the roughness function on realistic surfaces," J. Turbul. **15**, 350–365 (2014).

[29]J. Yuan, G. J. Brereton, G. Iaccarino, A. A. Mishra, and M. Vartdal, "Single-point structure tensors in rough-wall turbulent channel flow," in *Proceedings of the 2018 Summer Program* (2018).

[30]D. P. Zilker and T. J. Hanratty, "Influence of the amplitude of a solid wavy wall on a turbulent flow. part 2. separated flows," J. Fluid Mech. **90**, 257–271 (1979).

[31]J. Buckles, T. J. Hanratty, and R. J. Adrian, "Turbulent flow over large-amplitude wavy surfaces," J. Fluid Mech. **140**, 27–44 (1984).

[32]V. De Angelis, P. Lombardi, and S. Banerjee, "Direct numerical simulation of turbulent flow over a wavy wall," Phys. Fluids **9**, 2429–2442 (1997).

[33]E. Napoli, V. Armenio, and M. De Marchis, "The effect of the slope of irregularly distributed roughness elements on turbulent wall-bounded flows," J. Fluid Mech. **613**, 385–394 (2008).

[34]P. S. Jackson, "On the displacement height in the logarithmic velocity profile," J. Fluid Mech. **111**, 15–25 (1981).

[35]C. Maas and U. Schumann, "Direct numerical simulation of separated turbulent flow over a wavy boundary," in *Flow Simulation with High-Performance Computers II* (Vieweg+ Teubner Verlag, 1996) pp. 227–241.

[36]J. D. Hudson, *The effect of a wavy boundary on turbulent flow*, Ph.D. thesis, University of Illinois (1993).

[37]D. S. Henn and R. I. Sykes, "Large-eddy simulation of flow over wavy surfaces." J. Fluid Mech. **383**, 75–112 (1999).

[38]C. J. Keylock, K. S. Chang, and G. S. Constantinescu, "Large eddy simulatiojn of the velocity-intermittency structure for flow over a field of symmetric dunes," J. Fluid Mech. **805**, 656–685 (2016).

[39]J. Sillero, J. Jimenez, and R. D. Moser, "Two-point statistics for turbulent boundary layers and channels at Reynolds numbers up to $\delta^+ \approx 2000$," Phys. Fluids **26** (2014).

[40]M. R. Raupach and R. H. Shaw, "Averaging procedures for flow within vegetation canopies," Bound.-Lay. Meteorol. **22**, 79–90 (1982).

[41]O. Coceal, T. G. Thomas, and S. E. Belcher, "Spatial variability of flow statistics within regular building arrays," Bound.-Lay. Meteorol. **125**, 537–552 (2007).

[42]D. Pokrajac, I. McEwan, and V. Nikora, "Spatially averaged turbulent stress and its partitioning," Exp. Fluids **45**, 73–83 (2008).

[43]E. Mignot, E. Bartheleemy, and D. Hurther, "Double-averaging analysis and local flow characterization of near-bed turbulence in gravel-bed channel flows," J. Fluid Mech. **618**, 279–303 (2009).

[44]F. S. Stylianou, R. Pecnik, and S. C. Kassinos, "A general framework for computing the turbulence structure tensors," Comput. Fluids **106**, 54–66 (2015).

[45]F. S. Stylianou, R. Pecnik, and S. C. Kassinos, "Analyzing a turbulent pipe flow via the one-point structure tensors: Vorticity crawlers and streak shadows," Comput. Fluids **140**, 450–477 (2016).

[46]R. Mittal and G. Iaccarino, "Immersed boundary methods," Annu. Rev. Fluid Mech. **37**, 239–261 (2005).

[47]M. Vartdal, "Computing turbulence structure tensors in plane channel flow," Comput. Fluids **136**, 207–211 (2016).

667 [48]E. A. Fadlun, R. Verzicco, P. Orlandi, and J. Mohd-Yusof, "Combined immersed-boundary
668 finite-difference methods for three-dimensional complex flow simulations," J. Comput. Phys.
669 **161**, 35–60 (2000).
670 [49]N. Wood and P. Mason, "The pressure force induced by neutral, turbulent flow over hills." Q. J.
671 Roy. Meteor. Soc. **119**, 1233–1267 (1993).
672 [50]D. Pokrajac, L. J. Campbell, V. Nikora, and I. Manes, C. adn McEwan, "Quadrant analysis of
673 persistent spatial velocity perturbations over square-bar roughness," Exp. Fluids **42**, 413–423
674 (2007).
675 [51]R. J. Smalley, S. Leonardi, R. A. Antonia, L. Djenidi, and P. Orlandi, "Reynolds stress
676 anisotropy of turbulent rough wall layers," Exp. Fluids **33**, 31–37 (2002).
677 [52]A. Busse and N. D. Sandham, "Parametric forcing approach to rough-wall turbulent channel
678 flow," Journal of Fluid Mechanics **712**, 169–202 (2012).
679 [53]K. A. Flack and M. P. Schultz, "Roughness effects on wall-bounded turbulent flows," Phys.
680 Fluids **26**, 101305 (2014).
681 [54]S. Talapatra and J. Katz, "Coherent structures in the inner part of a rough-wall channel flow
682 resolved using holographic PIV," J. Fluid Mech. **711**, 161–170 (2012).
683 [55]P. Orlandi and S. Leonardi, "Direct numerical simulation of three-dimensional turbulent rough
684 channels: parameterization and flow physics," J. Fluid Mech. **606**, 399–415 (2008).
685 [56]S. Banerjee, R. Krahl, F. Durst, and C. Zenger, "Presentation of anisotropy properties of turbu-
686 lence, invariants versus eigenvalue approaches," J. Turbul. **8**, N32 (2007).
687 [57]R. L. Simpson, "Turbulent boundary-layer separation," Annu. Rev. Fluid Mech. **21**, 205–34
688 (1989).
689 [58]R. Martinuzzi and C. Tropea, "The flow around surface-mounted, prismatic obstacles placed in
690 a fully developed channel flow," ASME J. Fluids Eng. **115**, 85–92 (1993).
691 [59]P. A. Durbin, "A Reynolds stress model for near-wall turbulence," J. Fluid Mech. **249**, 465–498
692 (1993).
693 [60]G. J. Brereton and J. Yuan, "Wall-roughness eddy viscosity for Reynolds-Averaged closures,"
694 Int. J. Heat Fluid Fl. **73**, 74–81 (2018).
695 [61]S. C. Kassinos, C. A. Langer, S. L. Haire, and W. C. Reynolds, "Structure-based turbulence
696 modeling for wall-bounded flows," Int. J. Heat Fluid Flow **21**, 599–605 (2000).